Supporting Information

Linkages between GRACE Water Storage, Hydrologic Extremes, and Climate Teleconnections in Major African Aquifers

Bridget R. Scanlon[1], Ashraf Rateb[1], Assaf Anyamba[2], Seifu Kebede[3], Alan M. MacDonald[4], Mohammed Shamsudduha[5], Jennifer Small[2], Alexander Sun[1], Richard G. Taylor[5], and Hua Xie[6]

[1]Bureau of Economic Geology, Jackson School of Geosciences, University of Texas at Austin, Austin, Texas, USA

[2]NASA/Goddard Space Flight Center, Greenbelt, Maryland, USA

[3]Centre for Water Resources Research, University of KwaZulu-Natal (UKZN), South Africa.

[4]British Geological Survey, Lyell Centre, Edinburgh, United Kingdom

[5]Department of Geography, University College London, London, UK

[6] Environment and Production Technology Division, International

30 Pages

Two Sections

16 Figures

List of Figures

Acronyms

ID	ACRONYM	ABBREVIATION
1	AMO	Atlantic Multidecadal Oscillation
2	CHIRPS	Climate Hazards group InfraRed Precipitation with Stations
3	CLSM-F2.5	Catchment LSM-Fortuna 2.5
4	CPA	Cumulative Precipitation Anomaly
5	CRU	Climate Research Unit
6	CSEOF	CycloStationary Empirical Orthogonal Function
7	CSR.M	Center for Space Research Mascon
8	CT	Climate Teleconnection
9	DMI	Dipole Mode Index (Difference Between IOD.W &IOD.E)
10	ENSO	El Nino Southern Oscillation
11	GFZ	Geoforschungszentrum
12	GPCC	Global Precipitation Climatology Center
13	GRACE	Gravity Recovery and Climate Experiment
14	GSFC	Goddard Space Flight Center
15	GSWP3	Global Soil Wetness Project Phase 3
16	GW	Groundwater
17	GWS	Groundwater Storage
18	IMERG	Integrated Multi-Satellite Retrievals for GPM
19	IPO	Tripole Index for the Interdecadal Pacific Oscillation
20	JPL.M.dsf	Nasa Jet Propulsion Laboratory Mascon, Dsf, Downscaling Factor, 3° To 0.5° Grids.
21	LSM	Land Surface Models
22	MODIS	Moderate Resolution Imaging Spectroradiometer
23	NAO	North Atlantic Oscillation
24	NDVI	Normalized Difference Vegetation Index
25	Nino-3.4	Eastern Tropical Pacific Nino 3 – 4 Regions
26	Nino-ELI	ENSO Longitude Index (ELI)
27	Nino.04	Central Tropical Pacific, Nino 04 Region
28	Nubian	Nubian Aquifer System
29	P	Precipitation
30	PDO	Pacific Decadal Oscillation
31	QBO	Quasi-Biennial Oscillation (QBO) (A tropical, lower stratospheric)
32	SH	Spherical Harmonics
33	SM	Soil Moisture
34	SPEI	Standardized Precipitation Evapotranspiration Index
35	SSA	Sub-Saharan Africa
36	STL	Seasonal Trend Decomposition Using LOESS
37	SW	Surface Water

38	TIVR	Trend to Interannual Variability Ratio
39	TWS	Total Water Storage
40	VIC	Variable Infiltration Capacity Model
41	WGHM	WaterGAP Global Hydrological Model

1. Data

1.1. Total water storage (TWS)

Total water storage (TWS) variability data were derived from GRACE (Gravity Recovery and Climate Experiment) and GRACE-FO (Follow-On) satellite data. TWS anomalies (TWSAs) represent variations in TWS relative to the long-term monthly mean (2002 – 2020). Terrestrial TWS includes surface water, soil water, and groundwater. GRACE missions monitor temporal variability in the Earth's gravity field at monthly timescale and a spatial resolution of ~330 km. Temporal variations in Earth's gravity at regional and global scales is controlled primarily by variations in terrestrial water storage related to floods, droughts, and groundwater pumping. In this study GRACE data were based primarily on the ensemble mean of two mascon solutions: one from the University of Texas Center for Space Research (CSR-M) [1] and the other from NASA Jet Propulsion Lab (JPL-M) [2, 3]. Uncertainties in GRACE TWSAs are based on the standard deviation of the two mascon solutions and three Spherical Harmonic (SH) solutions from CSR, JPL, and GeoForschungsZentrum (GFZ) center. All data are available from April 2002 through July 2020 (no data form July 2017 – May 2018). All GRACE solutions were corrected for contributions from the atmosphere, oceans, tides, and Glacial Isostatic Adjustment (GIA) [4]. In addition, low degree coefficients (C_{20}, C_{21}, C_{22}, C_{30} (GRACE after August 2016 and GRACE-FO)) were replaced with other estimates from the satellite laser ranging system [5-7].

Mascon solutions are inspired by Bayes theorem by implementing prior knowledge on the distributions of the geophysical signal on the land and the ocean to constrain the estimates of mass fluxes from K-Band Range Rate (KBRR) data. CSR mascons use a geodetic grid based on the Tikhonov regularization technique and provide data using hexagonal tiles at a grid resolution of 0.25° [1]. JPL-M uses altimetry observations and geophysical models to constrain the mass flux and parameterize the gravity field using 3° spherical blocks [2]. JPL-M applies a coastline filter to attenuate the signal between the land and the ocean and applies a scaling factor based on the Community Land Model (CLM-4) [8] to restore signals that have been weakened through filtering less than 3° on land [9]. The data are then downscaled to 1° using CLM-4 and resampled at 0.5°. Even though the mascon solutions are available at higher resolutions (0.5° and 0.25°) the geophysical inferences of mass changes should be limited to the mission native resolution ~300 km, not at the downscaled resolution. Mascon solutions represent improvements in the quality of the GRACE data relative to the SH solutions (e.g. minimizing leakage errors, reducing highly correlated errors, and increasing signal recovery) [10]. The five GRACE solutions are centralized relative to their record (2002-2020).

SH solutions represent the traditional solutions of the GRACE missions. Besides applying the aforementioned corrections, decorrelation filters are applied to the solutions to attenuate the N-S stripes of the high degree SH. These stripes do not represent a geophysical phenomenon but result from the poor distributions of the GRACE satellites E-W ground tracking. The remaining errors are removed with a 300-km wide Gaussian filter [11]. Applying these filters leaks signal between the land to the ocean or among the pixels on land. The leakage problem is corrected by applying similar filters to global land surface models, which do not suffer from the N-S strips. The difference between the filtered and unfiltered solutions from the land surface models is then used to calculate scaling factors to restore the leaked signal in the GRACE SH solutions. The CLM-4 model [8] was used to obtain scaling factors for the three SH solutions

The gap between the GRACE mission (04/2002 -06/2017) and the GRACE-FO mission (05/2018-present) was not filled in this analysis because long-term variability is not affected by the 11 missing months. In addition, gap filling approaches require more external information from hydrological modeling and

ancillary data (e.g., precipitation, temperature) using statistical and machine learning framework, which is beyond the scope of the study.

We leverage the existing reconstructed climate-driven TWS data to inspect long-term historical variability in the Ogaden Juba and Upper Kalahari aquifers. These reconstructed data are based on the ensemble of JPL and NASA Goddard Space Flight Center (GSFC) mascons forced with the Global Soil Wetness Project Phase 2 project. **[**12**]**

The following URLs represent the accessible public domains for the GRACE data used in this study.

- UTCSR-M (GRACE/GRACE-FO - Gravity Recovery and Climate Experiment (utexas.edu)
- JPL-M.dsf(https://podaac.jpl.nasa.gov/dataset/TELLUS_GRAC-GRFO_MASCON_CRI_GRID_RL06_V2).
- SH solutions (Gravity Recovery and Climate Experiment (GRACE) Twin Satellites | PO.DAAC / JPL / NASA
- GRACE reconstucted data GRACE-REC: A reconstruction of climate-driven water storage changes over the last century (figshare.com)

1.2. Precipitation (P)

Four precipitation data sets are used in this study to evaluate changes in rainfall patterns over African aquifers at seasonal and interannual scales in addition to assessing relationships between rainfall and TWS variability and climate teleconnections.

1.2.1. Climate Hazards Group InfraRed Precipitation with Stations (CHIRPS)

CHIRPS data are available at 0.05° resolution and at monthly timescales for the Africa continent. CHIRPS was created to support the objectives of the United States Agency for International Development (USAID) Famine Early Warning Systems Network (FEWS NET) to provide relevant precipitation data (e.g., seasonal and drought monitoring and trend analyses) [13]. CHIRPS makes use of satellite data (e.g. Tropical Rainfall Measuring Mission Multi-Satellite Precipitation Analysis version 7 (TMPA 3B42 v7) and in-situ observations via the smart interpolation approach [13]. We used data from 1980 through 2020 at grid and aquifers scales in Africa. CHIRPS data are available through https://www.chc.ucsb.edu/data.

1.2.2. Integrated Multi-satellite Retrievals for GPM (IMERG)

IMERG data are based on integrating "all" precipitation products generated from microwave satellites, microwave-calibrated infrared (IR) satellites, gauges, and other potential estimators to obtain a finer resolutions product at 0.1° over the entire Earth, and from hourly to monthly time scales. Global Precipitation Mission (GPM) is a new international mission released by NASA and the Japan Aerospace Exploration Agency (JAXA) in 2014 as a follow on to the TRMM, which retired in 2015. GPM observes heavy rainfall, falling snow, and light rain and covers most of the world (latitudes +65°/-65°) [14]**.** The product used here is the monthly product for the data between 2000 and 2020. IMERG data are available through https://disc.gsfc.nasa.gov/datasets/GPM_3IMERGM_06/summary.

1.2.3. Climate Research Unit (CRU)

The CRU dataset is produced by the UK's National Centre for Atmospheric Science (NCAS) at the University of East Anglia's Climatic Research Unit for ten climate variables (e.g., precipitation, temperature, humidity) at a resolution of 0.5° between 1901-2018 and is based on in-situ observations. We included

the recent release of the CRU TSv4 for precipitation over Africa between 2002-2018 [15]. Data are freely available from https://crudata.uea.ac.uk/cru/data/hrg/.

1.2.4. Global Precipitation Climatology Centre (GPCC)

GPCC is a gridded dataset for rainfall based on in-situ observations and available at a resolution of 0.5° between 1901-2018 at monthly time scale. GPCC data are developed by Deutscher Wetterdienst (National Meteorological Service of Germany). The new product V.2020 is based on data from 84,800 stations for background climatology. The gridded analysis product is freely available through http://gpcc.dwd.de. We incorporated the data between 2000 and 2020 for this study.

1.3. MODIS (NDVI) and Land COVER

To assess variations in vegetation coverage related to precipitation, we evaluated the Moderate Resolution Imaging Spectroradiometer (MODIS) satellite products for canopy greenness leaf area, which is represented by the Normalized Difference Vegetation Index (NDVI). NDVI data are available at a resolution of 250 m and temporal sampling of 16 days based on daily derivatives of the atmosphere bidirectional surface reflectance [16].

In addition to NDVI, we also examined land cover using an annual product of land cover dynamics, which characterizes three non-vegetation classes and 11 vegetation classes based on the classification of five land cover schemes using a Machine learning algorithm (e.g., decision tree). The products are generated bi-annually (Jun-July) and (December-January), accounting for the differences in the growing seasons in both hemispheres. Data for the NDVI and land cover are available through (MODIS Land Team Home Page (nasa.gov)).

1.4. Climate Teleconnections

To account for the impact of climate variability on TWS variability, precipitation change, and vegetation indices in Africa over the past 40 years. We incorporated 10 climate teleconnection indices for the states of the oceans and seas surrounding Africa. The following URL includes the data sources for these indices (Climate Indices: Monthly Atmospheric and Ocean Time Series: NOAA Physical Sciences Laboratory).

List of the climate indices used in this study

ID	*Index*	
1	AMO	Atlantic Multidecadal Oscillation
2	NAO	North Atlantic Oscillation
3	PDO	Pacific Decadal Oscillation
4	IPO	Tripole Index for the Interdecadal Pacific Oscillation
5	Nino-3.4	Eastern Tropical Pacific SST, Nino 3 – 4 regions
6	Nino.04	Central Tropical Pacific SST, Nino 04 region
7	Nino-ELI	Nino ENSO Longitude Index (ELI)
8	DMI	Dipole Mode Index (difference between IOD.W & IOD E)
9	QBO	Quasi-biennial Oscillation (QBO) (a tropical, lower stratospheric)

1.5. Hydrological Models

In this section, we outline the land surface models (e.g., Global Land Data Assimilation System 2.1 of the NOAH-3.4 and the Catchment Land Surface Model (CLSM)) [17], and global hydrologic model (WaterGAP hydrological model) [18]. These models were used to calculate the groundwater storage (GWS) changes in the major aquifers in Africa

1.5.1. GLDAS 2.0 and 2.1 Models

GLDAS is a global high-resolution framework to simulate the states and process of the energy and water budgets by ingesting satellite data and in situ observations [19]. GLDAS was developed by the NASA Goddard Space Flight Center (GSFC) and National Oceanic and Atmospheric Administration (NOAA) National Center for Environmental Prediction (NCEP). GLDAS-2 has three frameworks 2.0, 2.1, 2.2. GLDAS 2.0 is forced entirely with the Princeton Global Meteorological Forcing Dataset [20] between 1948 and 2014. While version 2.1 is forced by observed data and models (e.g., Global Precipitation Climatology Project (GPCP) daily Analysis precipitation between 2001 and the present. Both version 2.0 and 2.1 are open-loop (no data assimilation) whereas version 2.2 makes use of the GRACE CSR.M data by assimilating TWSA into the CLSM model to better disaggregate TWSA into surface, root zone soil moisture, and groundwater. We used output from GLDAS 2.1 represented by two models (NOAH-3.4 and CLSM-F2.5) [21] with monthly resolution and 1° spatial resolution. Version 2.1 is forced with the Global Precipitation Climatology Project (GPCP) dataset. The NOAH model [22] has been operated by the NCEP since 1996, based on land surface schemes from the Oregon State University model. The land surface scheme includes explicit representation of soil hydrology, soil thermodynamics, and vegetation canopy. The estimates of SM in this model are based on summing the four soil layers to a depth of 2 m. The CLSM-F2.5 model differs from other LSMs by using catchment topography as the key to the land surface modeling instead of grids. The topographic index is also an expression of the water table depth using the TOPMODEL formulation [23]. The states of soil moisture, canopy, and groundwater are products of the catchment deficit defined as the amount of water required to saturate the catchment relative to the bedrock. The change in bedrock depth allows the dynamics of the TWS to be captured [24]. The recent model has a bedrock depth of ~2 m [24]. GLDAS 2.1 outputs can be accessed through https://ldas.gsfc.nasa.gov/gldas. The states of the SM

profile from the two models and the amount of the runoff from both models are included between 2002 and 2020 in this study to generate estimates for the GWS change in African aquifers

1.5.2. WGHM 2.2d

The LSMSs models do not simulate the components of the Surface Water Storage (SWS)which is the critical component in the water balance equation, but WGHM does. SWS in WGHM includes contributions from lakes, reservoirs, wetlands, rivers. The model version included in this study is the newest version available, WGHM-2.2d [18]. Improvements in the new model relative to the previous version (2.2) include use of updated versions of databases of global lakes, dams, and wetlands, which represent improvements in locations and areas of the surface water bodies. We incorporated the model outputs for the SW between 2002 and 2016 at monthly time scale and 0.5° spatial resolution. Outputs of the WGHM model are available through Müller Schmied, H et al. (2020): The global water resources and use model WaterGAP v2.2d - Standard model output (pangaea.de).

2. Methods

2.1. Seasonal Trend Decomposition using LOESS (STL)

The TWSA anomalies are decomposed using the Loess algorithm [25] into long term variability, oscillations (interannual, annual, and semiannual), and residuals.

$$S_{Raw} = S_{Long-term} + S_{Annual} + S_{Semi-annua} + S_{Residual} \quad (1)$$

$$S_{Long-term\ variability} = S_{Linear\ trend} + S_{Interannual\ variability} \quad (2)$$

During the decomposition, the signal was first detrended and then the subseries smoothing (series of all January, etc.) is applied to the time series with given higher weight to the beginning of the time series and then interpolate the rest. Then a polynomial regression is applied with degree one or two to get the smoothed signal and followed by a low pass filter based on the weighted averaging. Thus, annual smoothing allows for a yearly varied cycle to some degree. The annual cycle is then removed, and the remainder smoothed to find the trend components. The process is iterated few times. The results are two components, the annual cycle and long-term variability, which includes the linear trend and interannual variations besides the residual. There are two subjective parameters in the STL application, which makes the derived annual and long-term variability are controlled and could result in differences across the same application. These parameters are the smoothing windows of the seasonal and trend components: they represent how rapidly the trend and annual cycle change). In this analysis, we forced the smoothing window for the seasonal component to be periodic, and trend window to 13 months, and locally fitted to 1-degree polynomial. To account for the semiannual, we apply STL two times; the first to derive the sub-annual at a trend window of 7 months, the semiannual then removed from the signal. In the second iteration, we apply STL to derive the annual cycle only, and the long term component is decomposed using a nonparametric estimator (e.g., Theil Sen estimator [26]). The relative contribution of each element is calculated as the ratio of the variance of the component to the variance of the raw signal. STL has been applied in many GRACE TWSA studies (e.g., [27-31]).

2.2. Cyclostationary Empirical Orthogonal Functions (CSEOF)

Cyclostationary (time-dependent statistical properties) empirical orthogonal function analysis describes the temporal evolution of the eigenfunctions in eigenvalue problems that dominate many variables in the climate system by relaxing the stationarity assumption [32, 33]. In this sense, the method differs from other techniques (e.g., independent component analysis, complex EOF, and principal oscillation patterns) which founded on the assumption of the stationarity of the underlying physical process

To derive principal components based on the CSEOF, let's assume a physical process (e.g., TWS evolution on land or ENSO evolution in the ocean). The physical process ($B(t)$) is modulated by stochastic stationary amplitude $S(t)$ time series:

$$T(t) = B(t)S(t) \quad (3)$$

However, the physical process oscillates naturally by a period (d) that impacts its first-moment statistics (mean and covariance kernel)

$$B(t) = B(t + d) \quad (4)$$

Given that many physical processes ($B_n(r,t)$ can operate at the same time, modulated independently by different amplitudes and are periodic; their covariance kernel ($T(r,t)$) can be written as

$$T(r,t) = \sum_n B_n(r,t)S_n(t) \quad (5)$$

By depicting the physical process in space and time, the space-time covariance kernel can be solved using the double Fourier transform of the covariance matrix.

As a result, the CSEOF analysis of the entire dataset can be written as

$$Data_{T(r,t)} = \sum_n B_n(r,t)T_n(t) \quad (6)$$

where $B_n(r,t)$ are the CSEOF loading vectors (CSLVs), and $T_n(t)$ are the corresponding principal components. Both loading vectors and PCs are independent (t). Therefore, the space-time dependencies are data-driven and reflect the physical process evolution. For detailed mathematical derivatives of CSEOF in 3-D and 1-D, we refer to [32-34].

One subjective parameter that has to be selected when applying CSEOF is the nested period of the mean and the kernel covariance of the data. This period cannot be known for all of the physical processes. A safe choice is to use the least common multiple of all periods for all of the physical processes (e.g., 12 months for monthly data or 365 days for daily data). Such periods are clearly pronounced in the climate system, with many variables with annual periodicity [34]. Here we apply the CSEOF analysis (eq. 5) to 1-D time series (detrended TWSA at the aquifer scale) and climate teleconnection indices based on a nested 12-month period. CSEOF analysis decomposes the single time series into 2-3 modes which explain up to 90%-95% of the variance. These modes represent the modulated annual cycle and the interannual to decadal variations in TWSA patterns of the climate indices. An example of CSEOF decomposition is given in Fig. S6 for five indices of the climate teleconnection.

CSEOF is used to explain the physical modes in TWSA based on GRACE data at a global scale [35], sea level rise [36, 37], and climate teleconnections [38].

2.3. Composite Analysis of Precipitation and Vegetation Indices

Composite analysis was applied to precipitation and NDVI data during the pronounced ENSO and DMI cycles between 1980 and 2020. The ENSO events were selected to be the months with anomalies >+1 for El Nino or <-1 for La-Nina events based on the ENSO-ELI index. During these 40 years, the climatology means (monthly mean of all January, etc.), based on CHIRPS data, were removed, and the monthly anomalies during these events were averaged to depict the anomaly patterns of the rainfall season during these events and the changes in vegetation across Africa. We selected the rainfall season (October, November, and December (OND)) which represents the high rainfall season during the year and the also coincident with peaks of the ENSO and IOD.

El-Nino years with OND >+1 or <-1 from ELI index that included in the composite analysis were 1982, 1997 and 2015, and La Nina years were 1998, 1999, 2008 and 2010.

2.4. Cross correlations

The lead/ lag relationship among TWSA, precipitation, and climate teleconnections was established by measuring the correlation among the results of the CSEOF, assuming If the TWSA or precipitation at aquifer scale is driven by specific climate teleconnection, the variations in the amplitude of the time series of both systems should be consistent at least. The cross-correlation calculated as

$$r(t) = \frac{\sum_{t=1}^{N}[(X^t-\bar{X})*(Y^t-\bar{Y})]}{\sqrt{\sum_{t=1}^{N}(X^t-\bar{X})^2}\sqrt{\sum_{t=1}^{N}(Y^t-\bar{Y})^2}} \quad (7)$$

whereX^t is the climate teleconnection signal, Y^t is the TWSA signal, $\bar{X}, \bar{Y}$ are the mean of the two signals, N is the number of lags.

The correlation values are evaluated using the p value and t-student test and provided in excel files for each aquifer.

2.5. Deriving Groundwater Storage and its Uncertainties

Groundwater storage (GWS) in African aquifers can be derived as the residual of water storage budget

$$GWSA = TWSA - SMSA - SWSA. \quad (8)$$

Where the TWSA is the ensemble anomalies of the total water storage based on CSR and JPL mascons, SMSA is the soil moisture anomalies based on GLDAS-2.1 models (NOAH and CLSM -F2.5), SWSA is the surface water storages computed as the accumulated runoff in GLDAS models or sum of the lakes, rivers, wetlands, reservoirs in WGHM models.

The uncertainty. In the GWS can be described as

$$\sigma_{GWS} = \sqrt{\sigma_{TWSA}^2 + \sigma_{SMSA}^2 + \sigma_{SWSA}^2} \quad (9)$$

σ_{TWS} was taken as the standard deviation in the long-term variability from the different estimates of the TWSA (CSR-M, JPL.M.dsf, CSR-SH, JPL-SH, and GFZ-SH). The uncertainty in SMS was based on the standard deviation (σ_{SMS}) of the long-term variability from the GLDAS models (NOAH-2.8, MOSAIC, and VIC-4.0.3). Uncertainties in surface water storage to be 15% of the signal.

2.6. Cumulative Precipitation Anomaly

Monthly precipitation based on IMERG data between 2000 and 2020 for each aquifer was used to calculate the cumulative precipitation anomaly (CPA) as follows:

1) remove the rainfall climatological mean, and

2) accumulate the residual according to;

$$CPA = \sum_{i=1}^{n} X - \bar{X} \quad (10)$$

where, I=1, n= total time period, X is the monthly precipitation, and the $\bar{X}$ is the climatological mean.

2.7. Standardized Precipitation Evapotranspiration Index (SPEI)

SPEI is a drought index based on the water balance (precipitation minus evapotranspiration) used to quantify the change in the climate conditions in the African aquifers. Input data for SPEI were obtained from monthly GLDAS-2.1 forcing data between 2000 and 2020. The probability density function (PDF) based on logistic distribution was calculated and fitted for each month in the time series and standardized to a Gaussian variate with variability of one and mean of zero. SPEI was calculated using different windows (1-12 months) to present the progress of the wet and dry cycles through the years. The wet and dry conditions can be classified based on the standardized values of the SPEI as follows.

Climate conditions under SPEI values.

SPEI	Climate Conditions
≥**2**	Extremely wet
1.5 to 1.99	Very Wet
1.00 to 1.49	Moderately wet
-0.99 to 0.99	Near Normal
-1.00 to -1.49	Moderately dry
-1.50 to - 1.99	Severely dry
≤ -2	Extremely dry

3. Figures

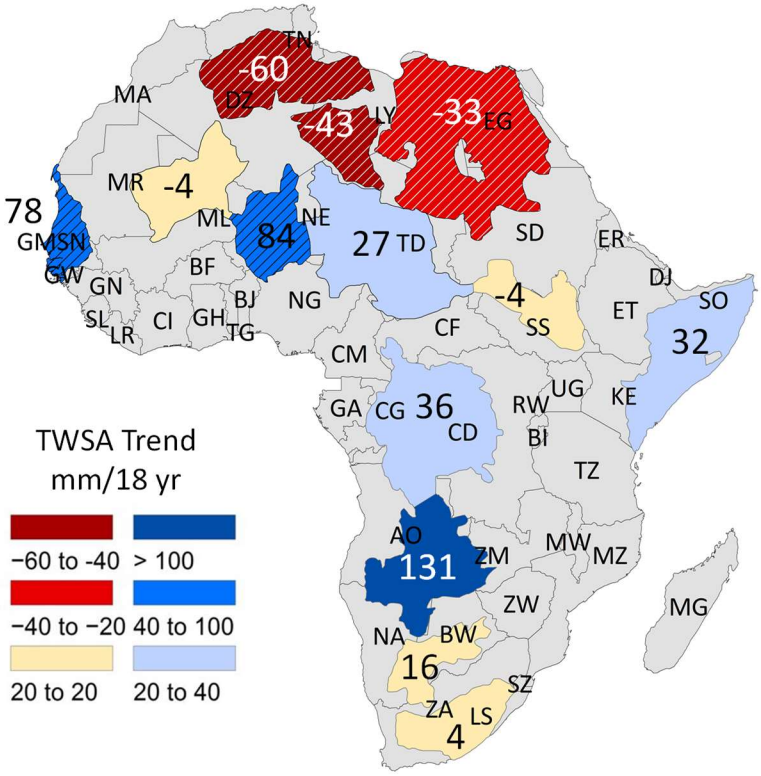

Figure S1. Linear trends in Total Water Storage Anomalies (TWSA) in mm over the 18 yr GRACE record in 13 major aquifers in mm over 18 yr GRACE record (2002 – 2020), corresponding to Fig. 1 which has trends in km^3 over 18 yr. Data are provided in Table S1.

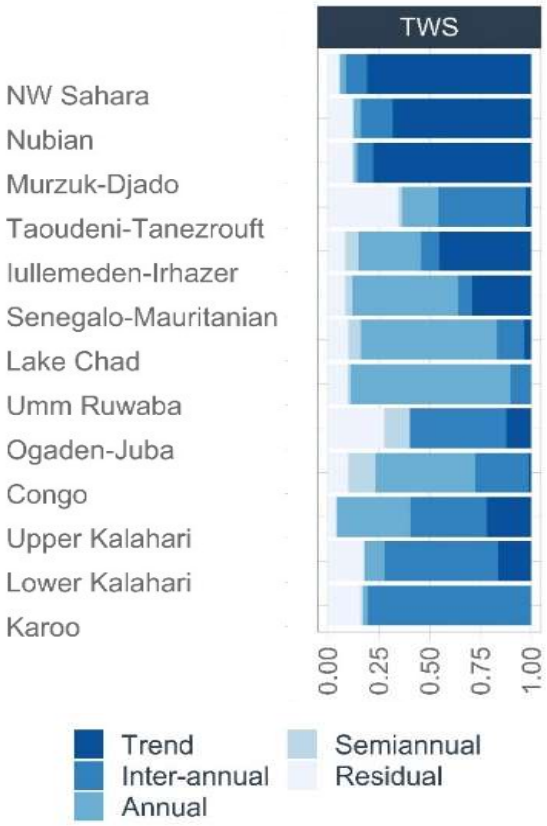

Figure S2. Component variances making up total variance in Total Water Storage, including linear trend, inter-annual, annual, semiannual, and residual components based on Seasonal Trend Decomposition using Loess (STL) analysis (Table S1a). Nubian refers to Nubian Aquifer System.

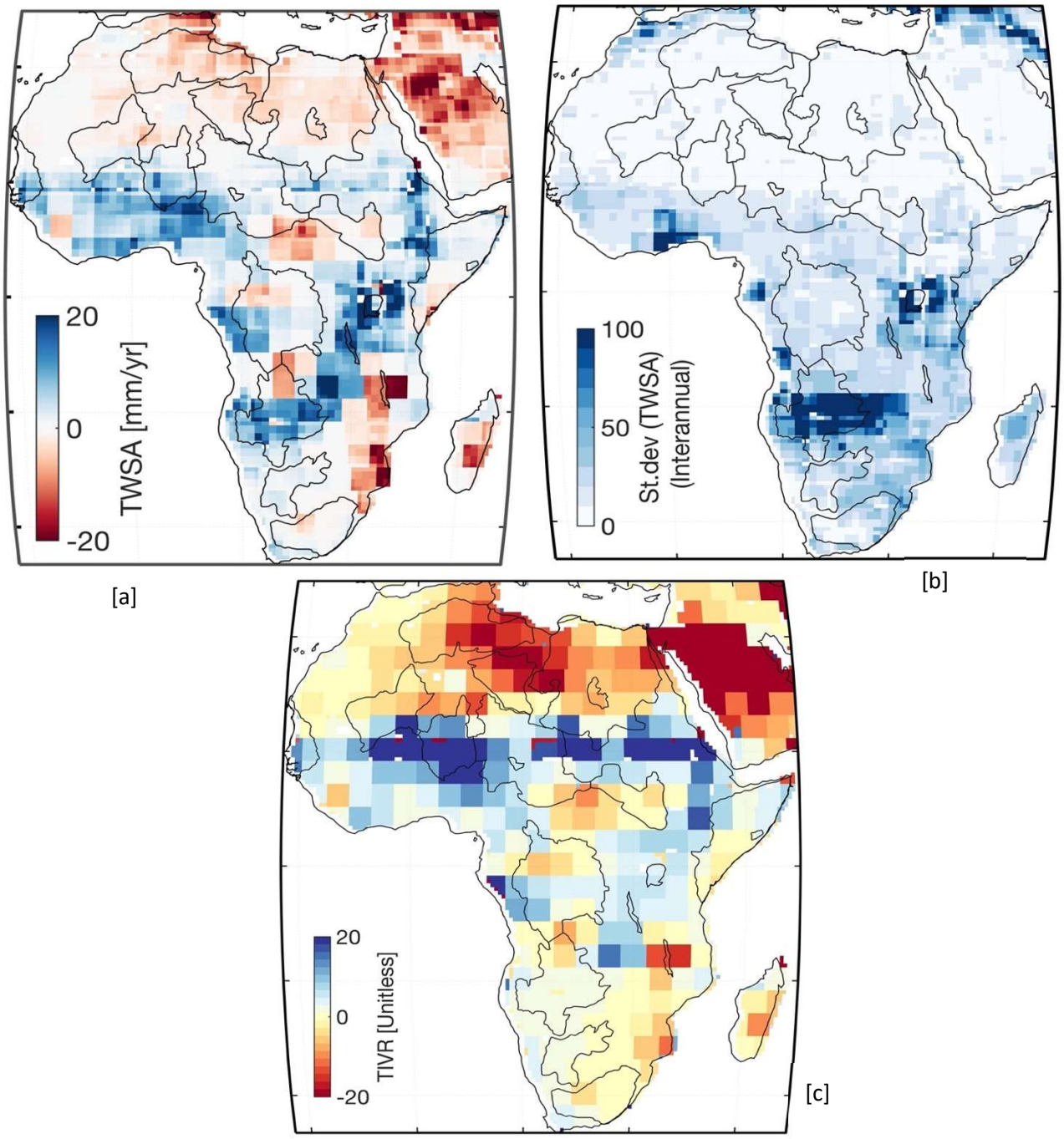

Figure S3. [a] Linear trend in GRACE and GRACE-FO TWS in Africa between 2002 and 2020 based on JPL mascon estimates; [b] Standard deviation of interannual TWS variability; and [c] Trend (net change in 18.3 yr) to interannual variability ratio (TIVR).

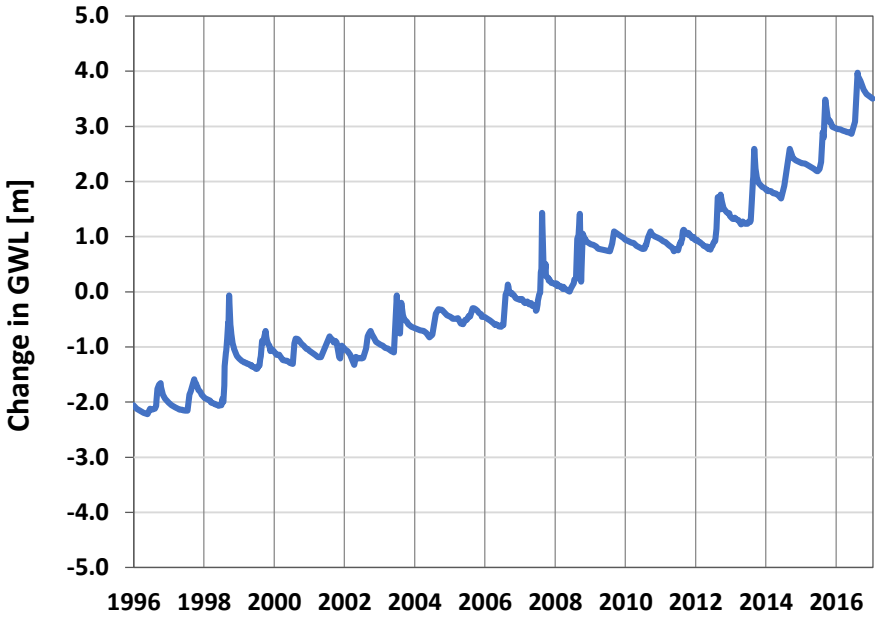

Figure S4. Change in groundwater level in well located in Niger, Banizoumbou (13.533°N, 2.662°E) in Iullemeden-Irhazer aquifer [39]. Data provided in Table S11.

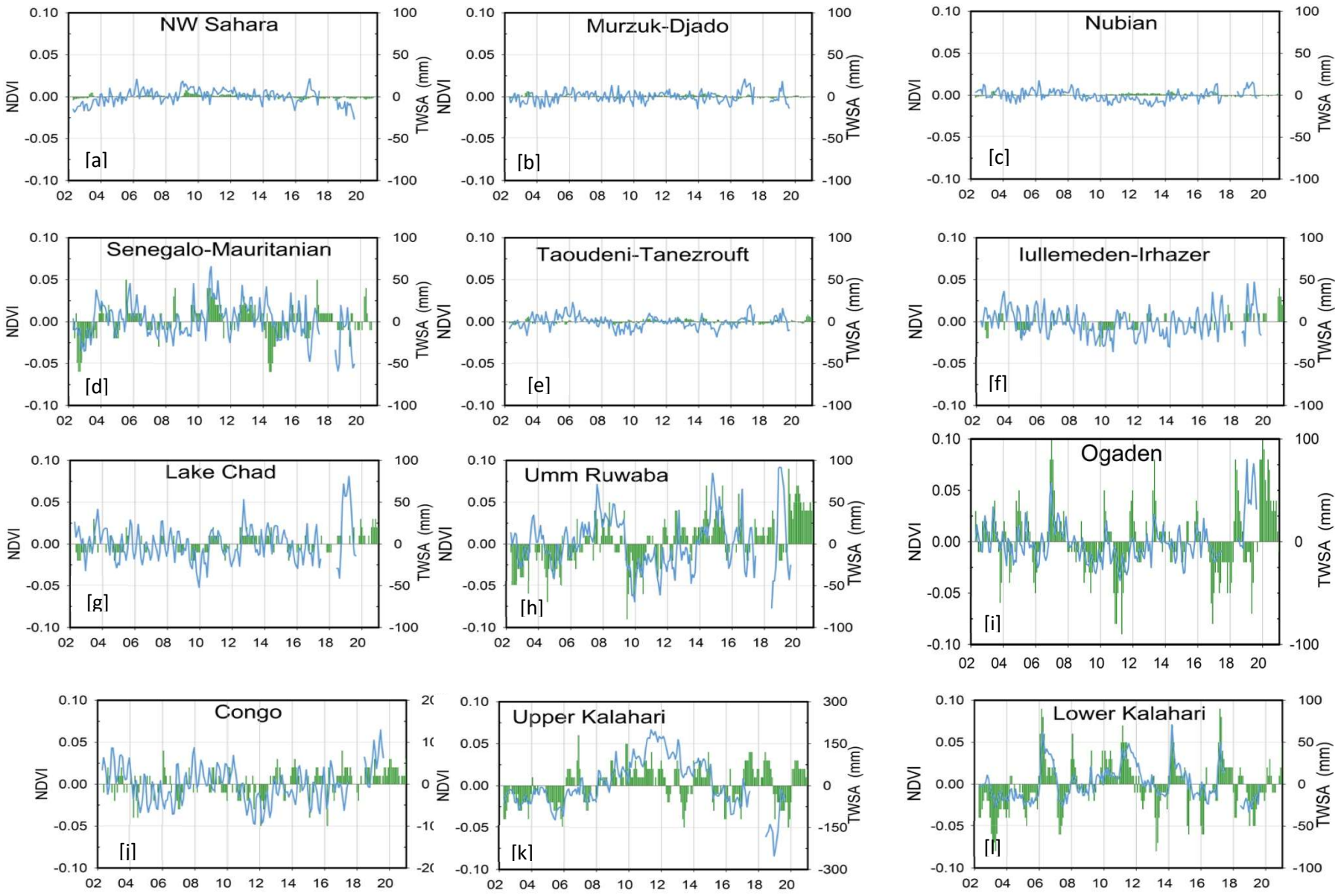
NW Sahara
[a]
Murzuk-Djado
[b]
Nubian
[c]
Senegalo-Mauritanian
[d]
Taoudeni-Tanezrouft
[e]
Iullemeden-Irhazer
[f]
Lake Chad
[g]
Umm Ruwaba
[h]
Ogaden
[i]
Congo
[j]
Upper Kalahari
[k]
Lower Kalahari
[l]
NDVI
TWSA (mm)
02 04 06 08 10 12 14 16 18 20

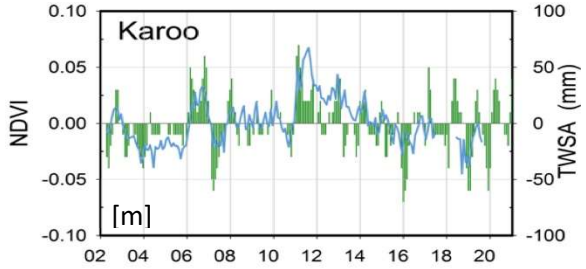

Figure S5. TWSAs from GRACE satellites and the normalized difference vegetations index (NDVI) after removing climatology from MODIS satellite in major African Aquifers. The correlations between TWSA and NDVI is presented in Table S1s. Data are provided in Table S7 (TWSA) and Table S22 (NDVI).

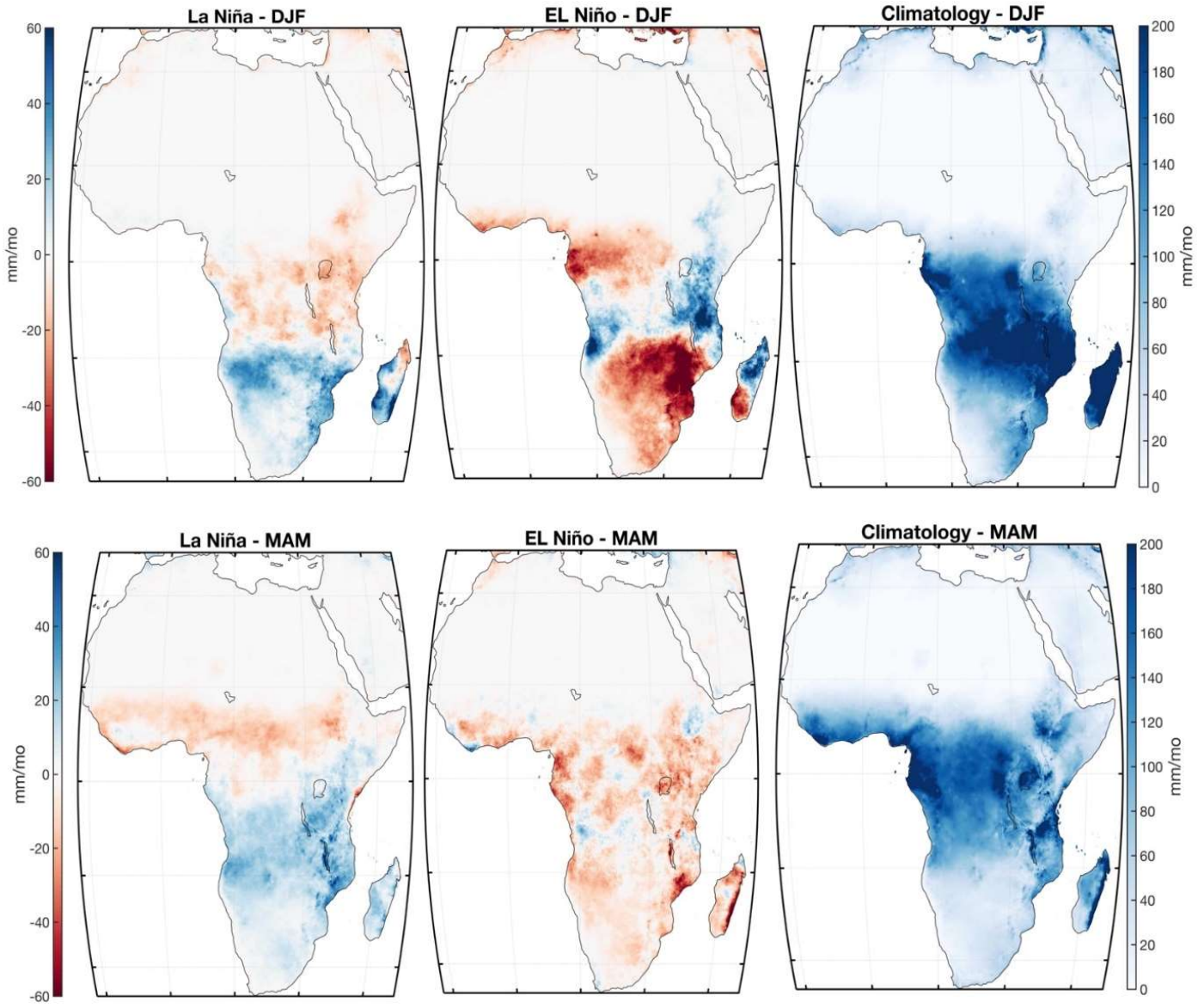
La Niña - DJF
EL Niño - DJF
Climatology - DJF
La Niña - MAM
EL Niño - MAM
Climatology - MAM
mm/mo
60
40
20
0
-20
-40
-60
200
180
160
140
120
100
80
60
40
20
0

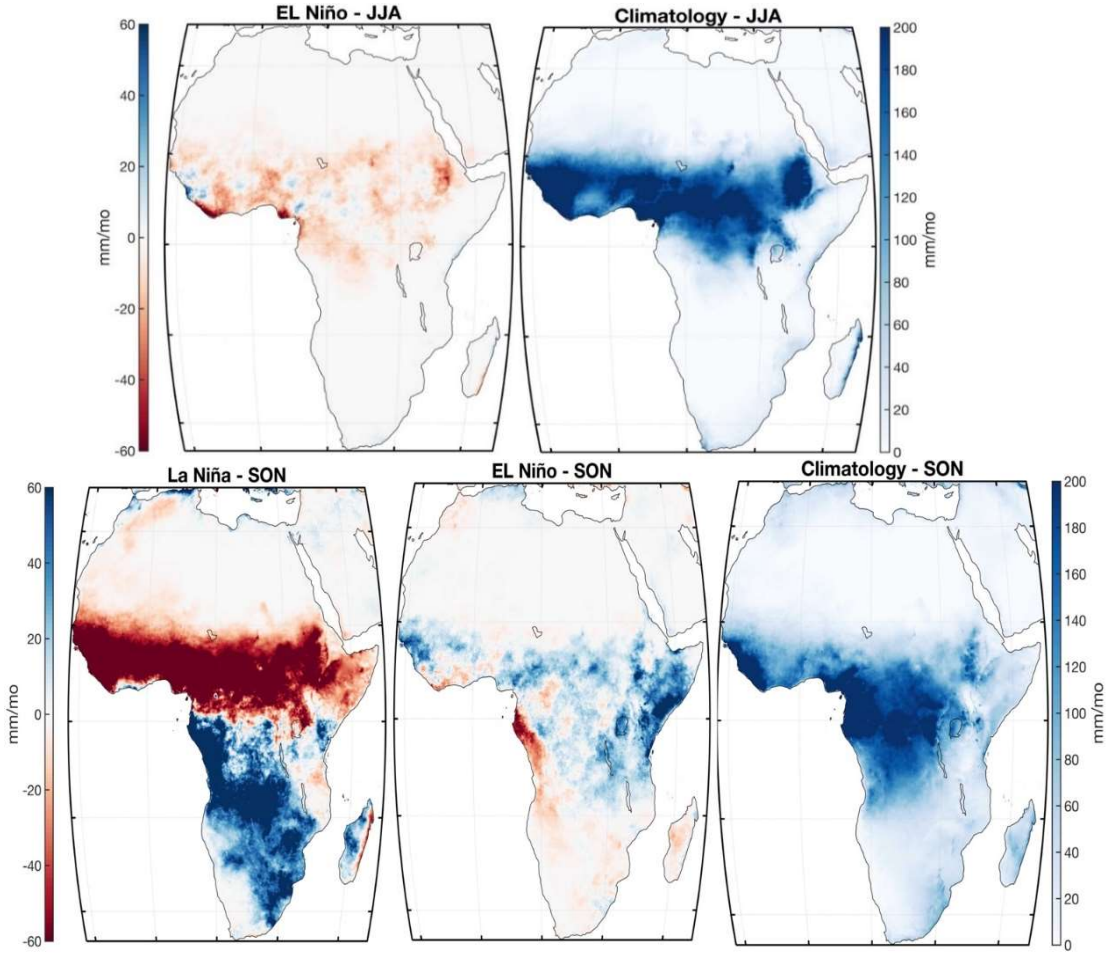

Figure S6. Composite map of rainfall anomalies in different climate seasons (DJF, MAM, JJA) during El Nino and La Nina years relative to the climatology based on rainfall between 1980 and 2020. ENSO events were selected based on ENSO-ELI (longitudinal index), reflecting the differences in eastern and central Pacific Ocean, ≥ 1 for El-Nino events, and $\leq -\mathbf{1}$ for La-Nina events for these months. El-Nino years for these selections include 1983; 1988, 1997, and 2015 and La-Nina years include 1998, 1999, 2008, and 2017. Results are based on CHIRPS rainfall data between 1980 and 2020.

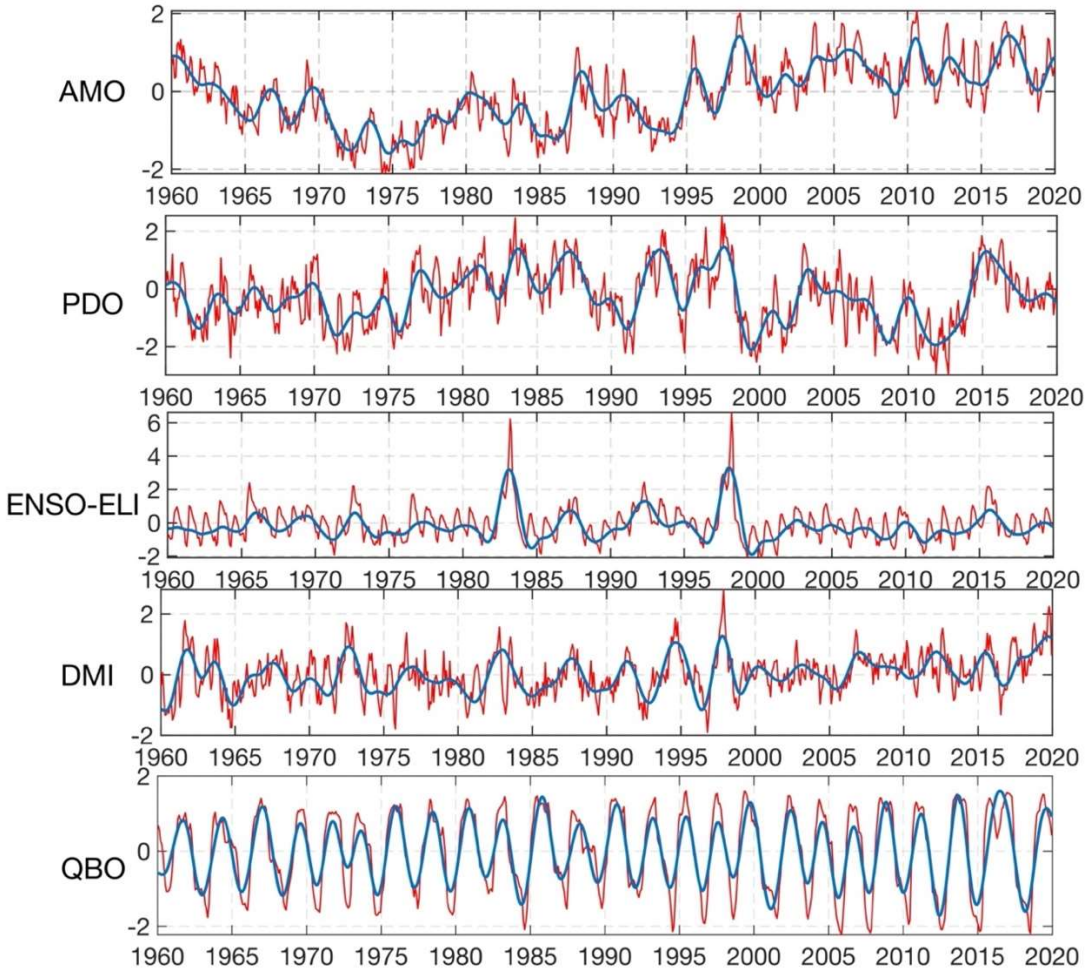

Figure S7. An example of CSEOF analysis for the climate teleconnections indices; red lines are raw time series, and blues lines are the reconstructed PC1 time series at a nested 12-month period. (Data are provided in Table S23).

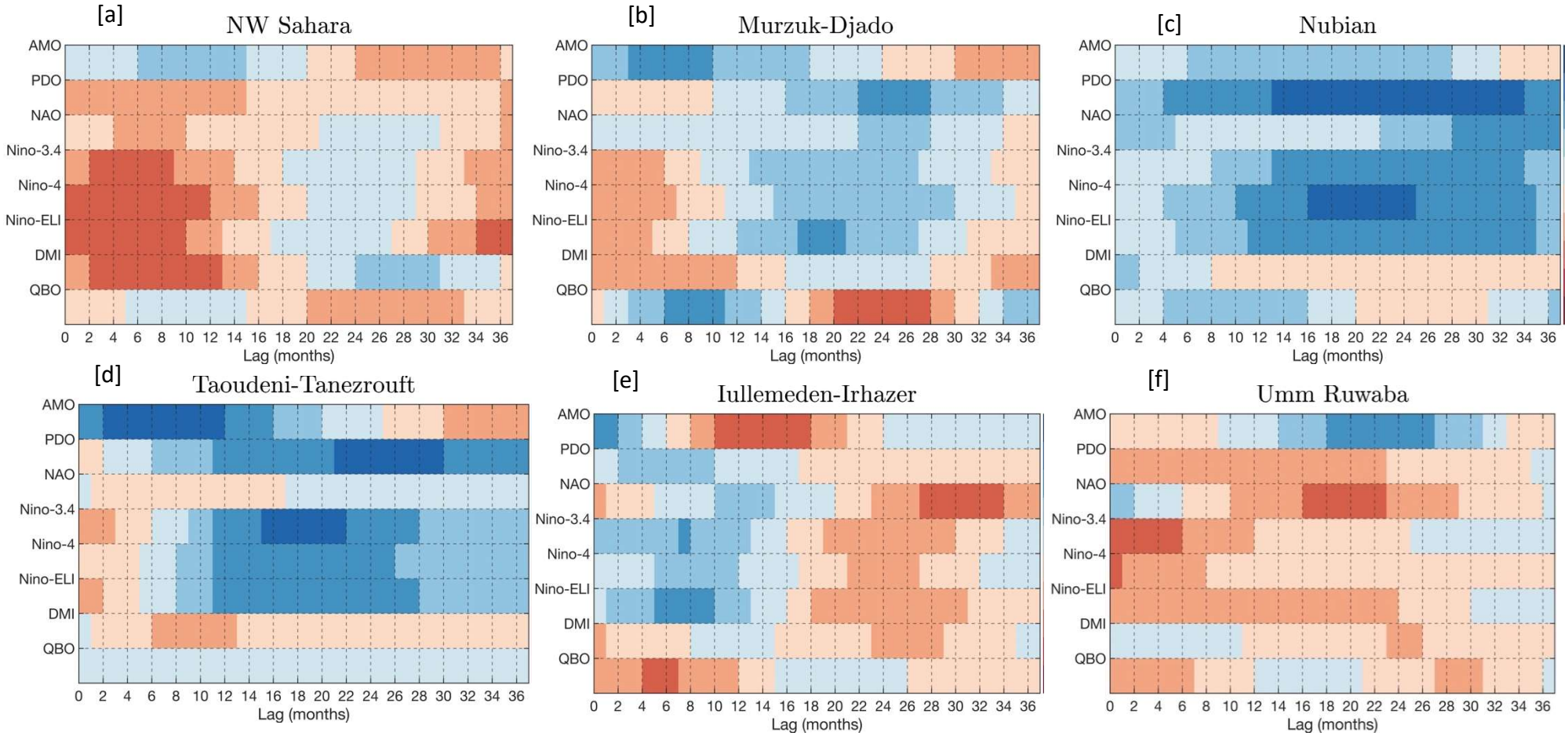
[a]
NW Sahara
[b]
Murzuk-Djado
[c]
Nubian
[d]
Taoudeni-Tanezrouft
[e]
Iullemeden-Irhazer
[f]
Umm Ruwaba
AMO
PDO
NAO
Nino-3.4
Nino-4
Nino-ELI
DMI
QBO
0 2 4 6 8 10 12 14 16 18 20 22 24 26 28 30 32 34 36
Lag (months)

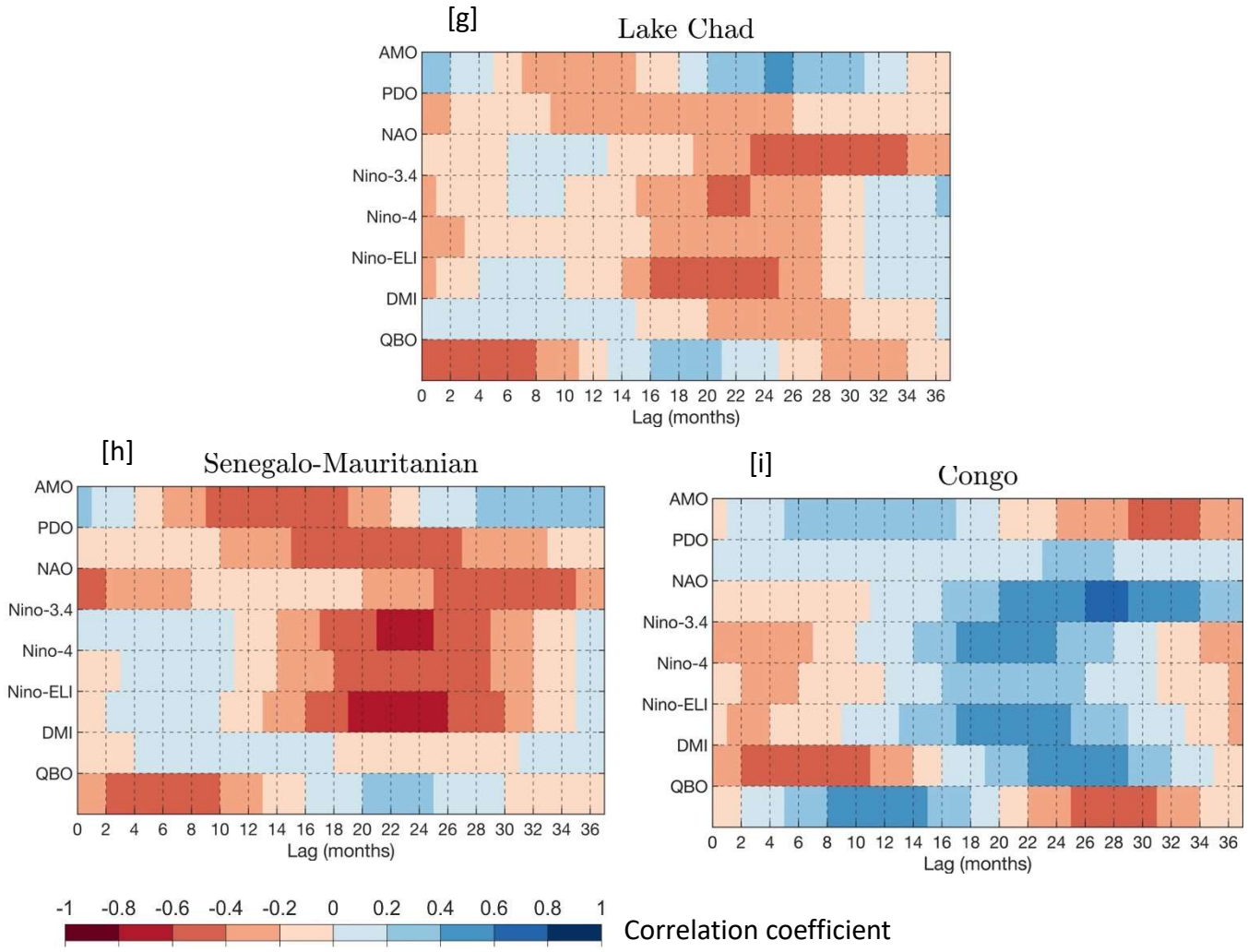

Figure S8. Significant cross correlation between the TWSAs and climate teleconnections based on principle components derived by the CSEOFs analysis for major aquifers in Africa. (Tables S23 – S25).

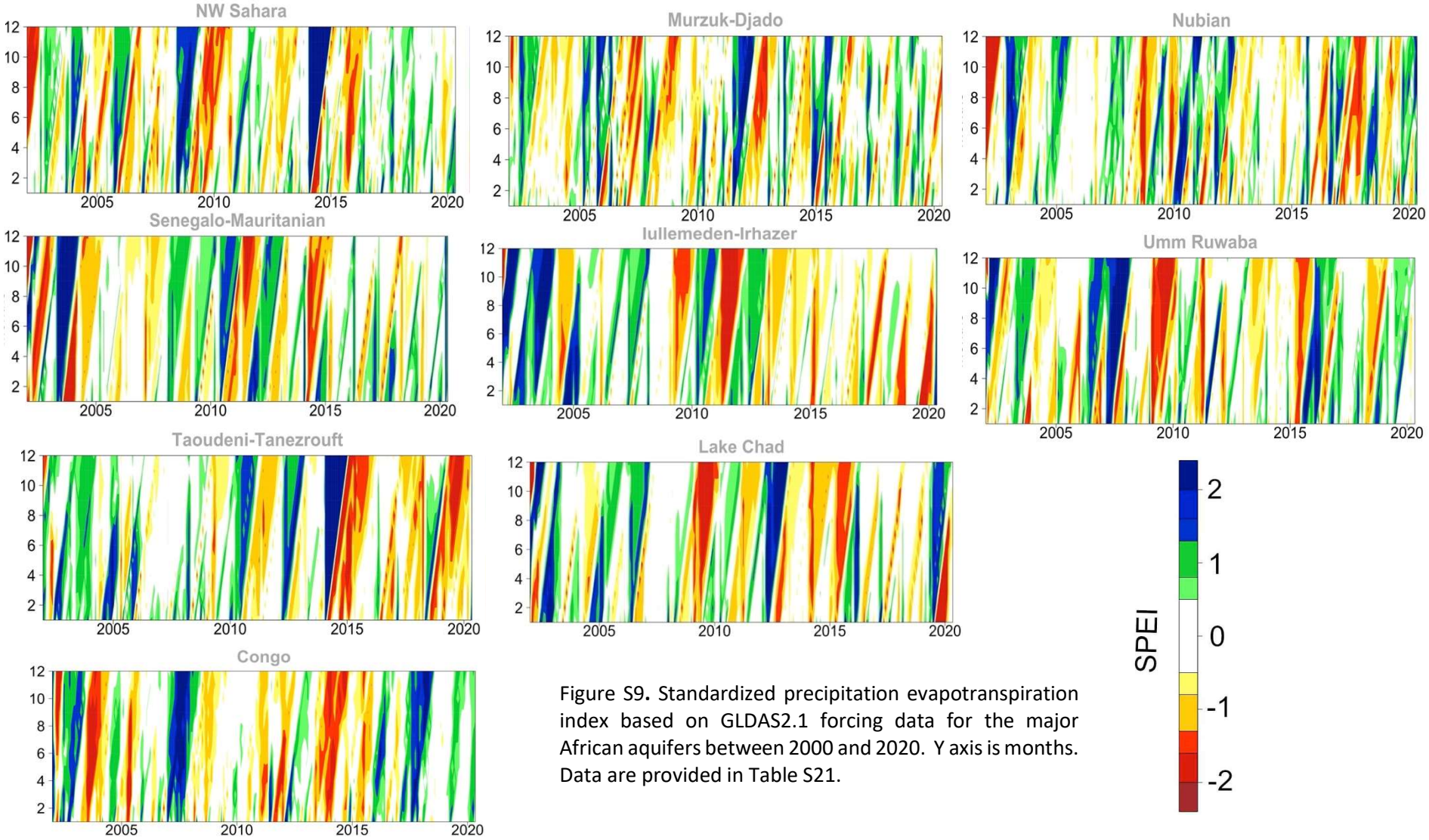

Figure S9. Standardized precipitation evapotranspiration index based on GLDAS2.1 forcing data for the major African aquifers between 2000 and 2020. Y axis is months. Data are provided in Table S21.

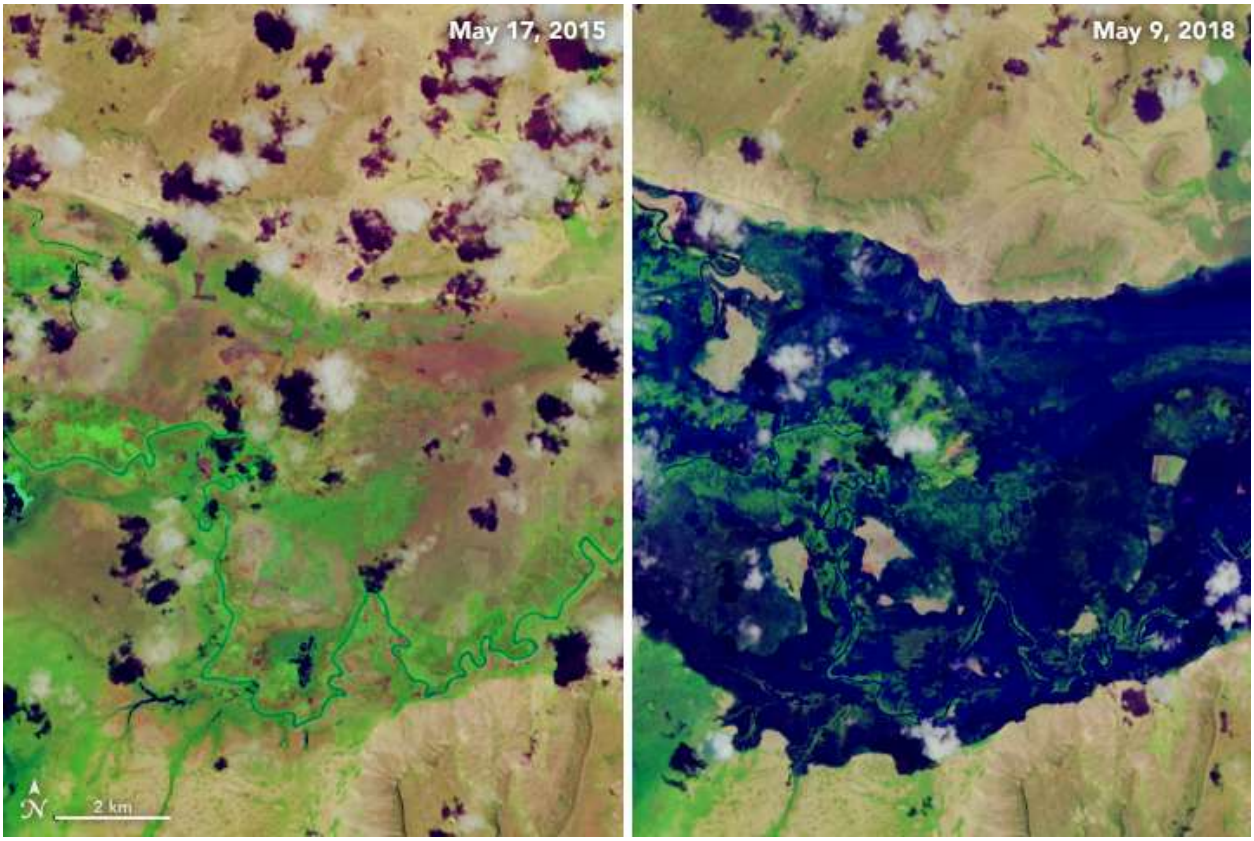

Figure S10. NASA images of the Shebelle River during a dry period (May 17, 2015) and wet period (May 9, 2018) [40]. Reproduced from NASA (2018). NASA Earth Observatory images by Joshua Stevens, using Landsat data from the U.S. Geological Survey and soil moisture data courtesy of JPL and the SMAP Science Team.

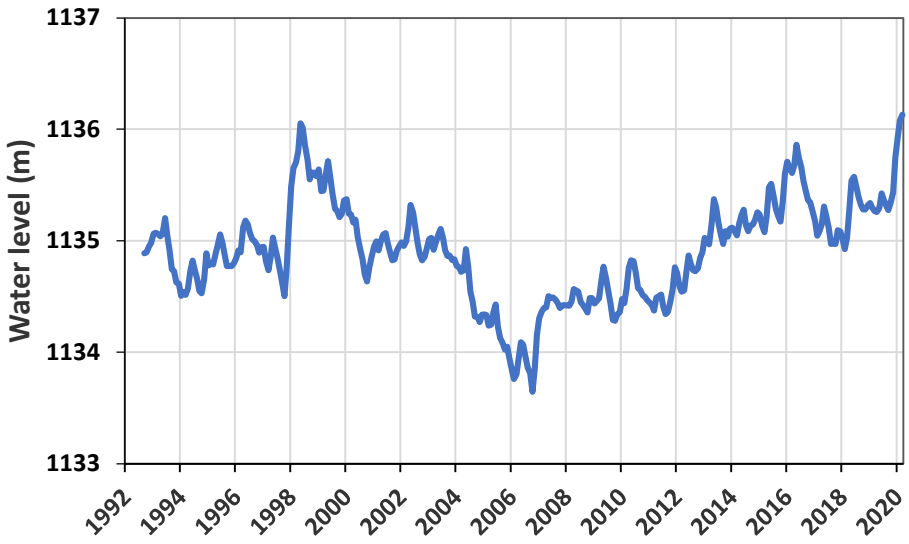

Figure S11. Water level change in Lake Victoria based on altimetry satellites (1992 – 2020) (Data provided in Table S27).

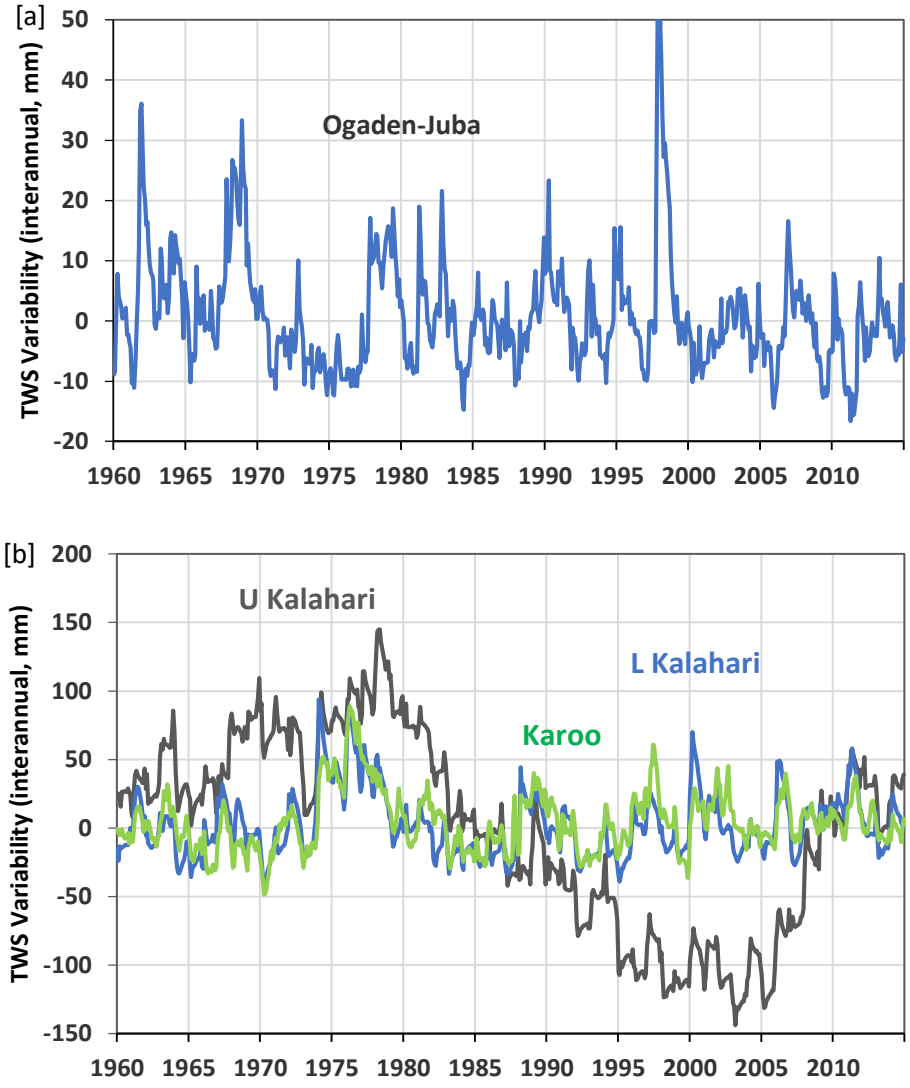

Figure S12. Reconstructed JPL-TWSA anomalies [12] in [a] Ogaden-Juba, and [b] Upper Kalahari, Lower Kalahari and Karoo aquifers (Table S13).

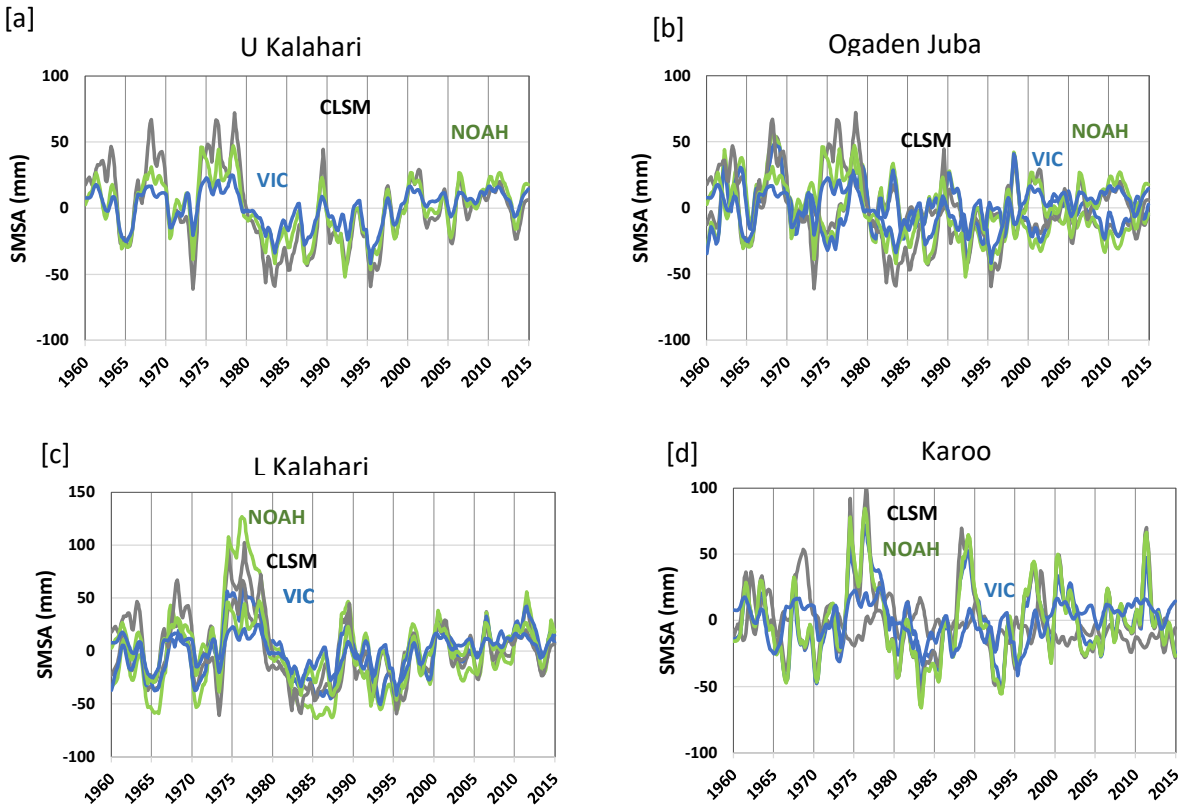

Figure S13. Long term variability of the soil moisture storage anomaly (SMSA, mm) in [a] Ogaden-Juba, [b] Upper Kalahari, [c] Lower Kalahari, and d [d] Karoo aquifers based on three GLDAS 2.0 models (CLSM, NOAH, and VIC). (Tables S14).

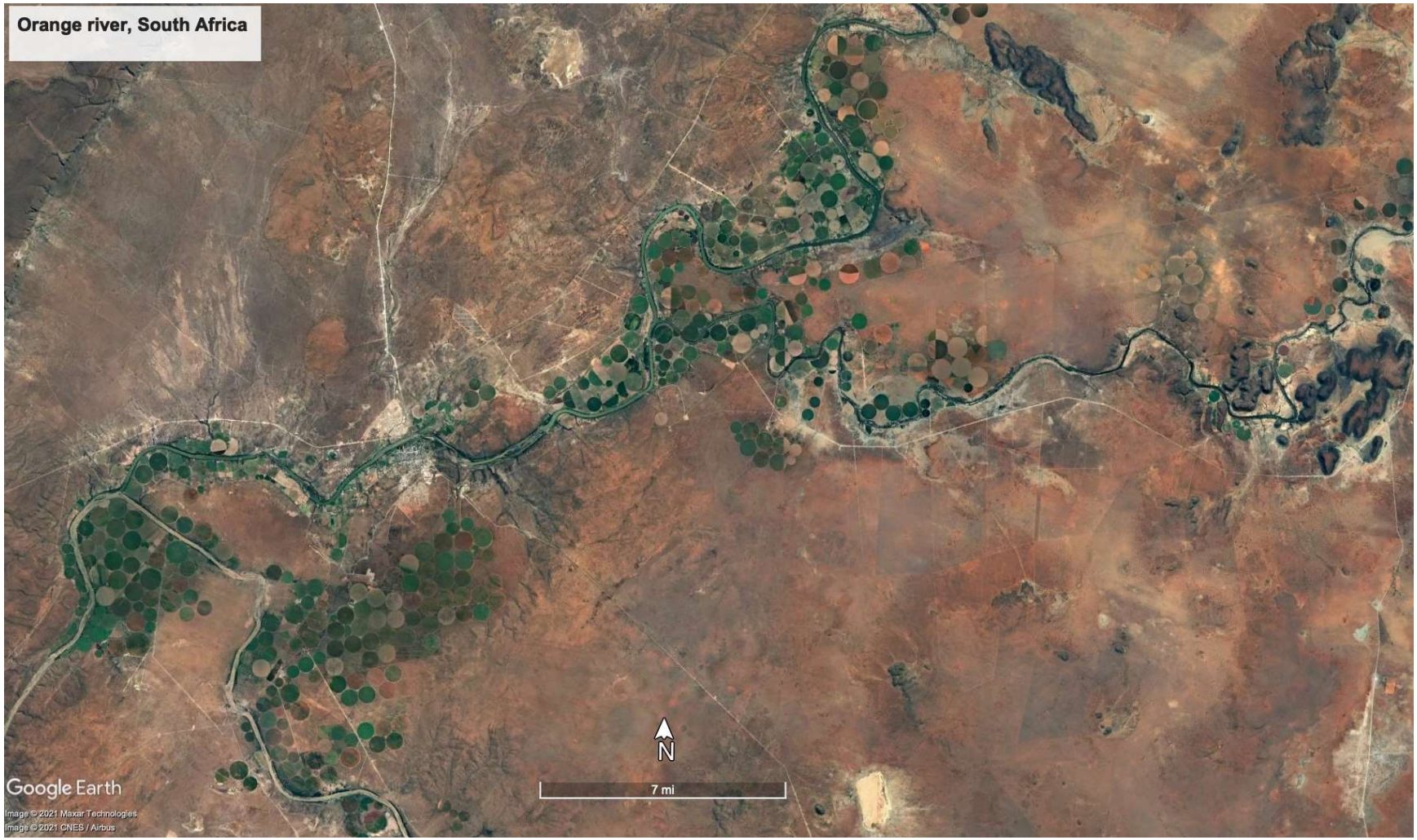

Figure S14. Google Earth image showing irrigated fields adjacent to Orange River. Image from November 11, 2021.

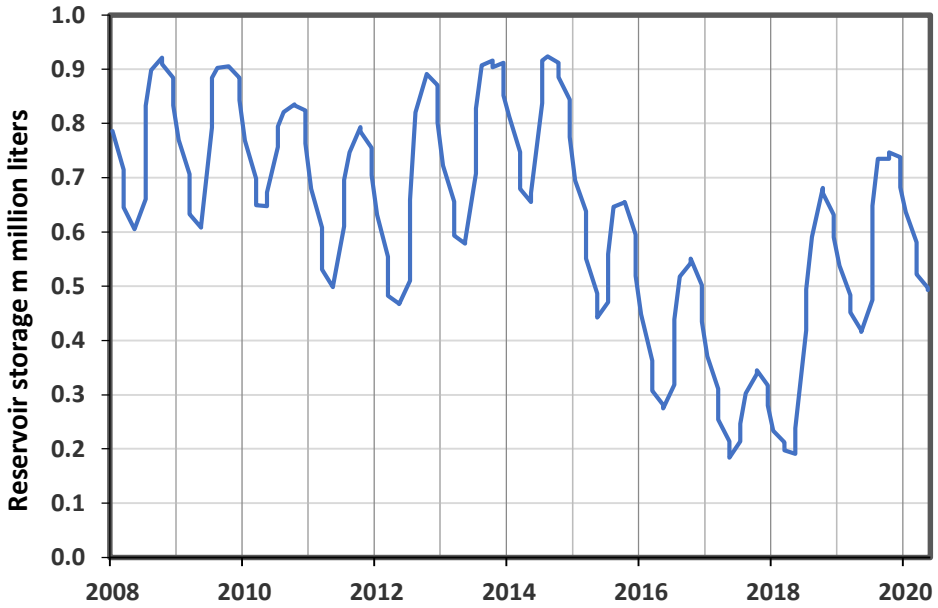

Figure S15. Reservoir storage in the major Western Cape Water Supply System (WCWSS) dams (Data are provided in Table S28).

Figure S16.Snapshot of the location of groundwater monitoring network in Africa, obtained from International Groundwater Resources Assessment Centre (IGRAC).

4. References:

1. Save, H., S. Bettadpur, and B.D. Tapley, *High-resolution CSR GRACE RL05 mascons.* Journal of Geophysical Research: Solid Earth, 2016. **121**(10): p. 7547-7569.
2. Watkins, M.M., et al., *Improved methods for observing Earth's time variable mass distribution with GRACE using spherical cap mascons.* Journal of Geophysical Research: Solid Earth, 2015. **120**(4): p. 2648-2671.
3. Wiese, D.N., F.W. Landerer, and M.M. Watkins, *Quantifying and reducing leakage errors in the JPL RL05M GRACE mascon solution.* Water Resources Research, 2016. **52**(9): p. 7490-7502.
4. Peltier , R., W., D.F. Argus, and R. Drummond, *Comment on "An Assessment of the ICE-6G_C (VM5a) Glacial Isostatic Adjustment Model" by Purcell et al.* Journal of Geophysical Research: Solid Earth, 2018. **123**(2): p. 2019-2028.
5. Sun, Y., R. Riva, and P. Ditmar, *Optimizing estimates of annual variations and trends in geocenter motion and J2 from a combination of GRACE data and geophysical models.* Journal of Geophysical Research: Solid Earth, 2016. **121**(11): p. 8352-8370.
6. Swenson, S., D. Chambers, and J. Wahr, *Estimating geocenter variations from a combination of GRACE and ocean model output.* Journal of Geophysical Research: Solid Earth, 2008. **113**(B8).
7. Landerer, F., *Monthly estimates of degree-1 (geocenter) gravity coefficients, generated from GRACE (04-2002-06/2017) adn GRACe-FO (06-2018 onwared) RL06 solutions.* GRACE Technical Note 13, The GRACE Project, NASA Jet Propulsion Laboratory (https://podaac-tools.jpl.nasa.gov/drive/files/allData/grace/docs/TN-13_GEOC_CSR_RL06.txt), 2019.
8. Landerer, F.W. and S.C. Swenson, *Accuracy of scaled GRACE terrestrial water storage estimates.* Water Resources Research, 2012. **48**(4).
9. Wiese, D.N., *GRACE monthly global water mass grids netcdf release 5.0. ver. 5.0. po.daac, ca, usa.dataset accesseed (2016-02004)), http://grace.jpl.nasa.gov/, doi:10.5067/TEMSC-OCL05.* 2015.
10. Scanlon, B.R., et al., *Global evaluation of new GRACE mascon products for hydrologic applications.* Water Resources Research, 2016. **52**(12): p. 9412-9429.
11. Swenson, S. and J. Wahr, *Post-processing removal of correlated errors in GRACE data.* Geophysical Research Letters, 2006. **33**(8): p. L8402.
12. Humphrey, V. and L. Gudmundsson, *GRACE-REC: a reconstruction of climate-driven water storage changes over the last century.* Earth System Science Data, 2019. **11**(3): p. 1153-1170.

13. Funk, C., et al., *The climate hazards infrared precipitation with stations—a new environmental record for monitoring extremes.* Scientific data, 2015. **2**(1): p. 1-21.

14. Huffman, G.J., et al. *GPM IMERG Final Precipitation L3 1 month 0.1 degree x 0.1 degree V06, Greenbelt, MD, Goddard Earth Sciences Data and Information Services Center (GES DISC)*. 2019 2021-05-29].

15. Harris, I., et al., *Version 4 of the CRU TS monthly high-resolution gridded multivariate climate dataset.* Scientific data, 2020. **7**(1): p. 1-18.

16. Didan, K. *MOD13Q1 MODIS/Terra Vegetation Indices 16-Day L3 Global 250m SIN Grid V006</i> [Data set]. NASA EOSDIS Land Processes DAAC.* . 2015 2021-05-30].

17. Koster, R.D., et al., *A catchment-based approach to modeling land surface processes in a general circulation model 1. Model structure.* J. Geophys. Res. Atmospheres, 2000. **105**(D20): p. 24809-24822.

18. Müller Schmied, H., et al., *The global water resources and use model WaterGAP v2. 2d: Model description and evaluation.* Geoscientific Model Development, 2021. **14**(2): p. 1037-1079.

19. Rodell, M., et al., *The global land data assimilation system.* Bull. Am. Meteor. Soc., 2004. **85**(3): p. 381-394.

20. Sheffield, J., G. Goteti, and E.F. Wood, *Development of a 50-year high-resolution global dataset of meteorological forcings for land surface modeling.* Journal of Climate, 2006. **19**(13): p. 3088-3111.

21. Beaudoing, H.K., M. Rodell, and NASA/GSFC/HSL. *GLDAS Noah Land Surface Model L4 monthly 1.0 x 1.0 degree V2.1, Greenbelt, Maryland, USA, Goddard Earth Sciences Data and Information Services Center (GES DISC)*. 2020 2021-05-30].

22. Chen, F., et al., *Modeling of land surface evaporation by four schemes and comparison with FIFE observations.* J. Geophys. Res. Atmos., 1996. **101 (D3)**: p. 7251-7268.

23. Beven, K.J. and M.J. Kirby, *A physically based variable contributing area model of basin hydrology.* Hydrol. Sci. Bull., 1979. **24**: p. 43-69.

24. Houborg, R., et al., *Drought indicators based on model-assimilated Gravity Recovery and Climate Experiment (GRACE) terrestrial water storage observations.* Water Resources Research, 2012. **48**.

25. Cleveland, R.B., W.S. Cleveland, and I. Terpenning, *STL: A seasonal-trend decomposition procedure based on loess.* Journal of Official Statistics, 1990. **6**(1): p. 3.

26. Sen, P.K., *Estimates of the regression coefficient based on Kendall's tau.* Journal of the American statistical association, 1968. **63**(324): p. 1379-1389.

27. Humphrey, V., L. Gudmundsson, and S.I. Seneviratne, *Assessing Global Water Storage Variability from GRACE: Trends, Seasonal Cycle, Subseasonal Anomalies and Extremes.* Surv Geophys, 2016. **37**(2): p. 357-395.

28. Scanlon, B., et al., *Global models underestimate large decadal declining and rising water storage trends relative to GRACE satellite data.* Proc Natl Acad Sci U S A, 2018. **115**(6): p. E1080-E1089.

29. Rateb, A., B.R. Scanlon, and K. Chung-Yen, *Multi-decadal Assessment of Water Resources in the Tigris-Euphrates Basin using Satellites, Hydrological Modeling, and In-situ Data* Science of The Total Environment, 2020.

30. Rateb, A., et al., *Comparison of Groundwater Storage Changes From GRACE Satellites With Monitoring and Modeling of Major U.S. Aquifers.* Water Resources Research, 2020. **56**(12): p. e2020WR027556.

31. Scanlon, B., et al., *Tracking seasonal fluctuations in land water storage using global models and GRACE satellites.* Geophysical Research Letters, 2019. **46**(10): p. 5254-5264.

32. Kim, K.-Y. and G.R. North, *EOFs of harmonizable cyclostationary processes.* Journal of the atmospheric sciences, 1997. **54**(19): p. 2416-2427.

33. Kim, K.-Y., G.R. North, and J. Huang, *EOFs of one-dimensional cyclostationary time series: Computations, examples, and stochastic modeling.* Journal of Atmospheric Sciences, 1996. **53**(7): p. 1007-1017.

34. Kim, K.-Y., B. Hamlington, and H. Na, *Theoretical foundation of cyclostationary EOF analysis for geophysical and climatic variables: concepts and examples.* Earth-science reviews, 2015. **150**: p. 201-218.

35. Hamlington, B., et al., *Amplitude Modulation of Seasonal Variability in Terrestrial Water Storage.* Geophysical Research Letters, 2019. **46**(8): p. 4404-4412.

36. Hamlington, B.D., et al., *Separating decadal global water cycle variability from sea level rise.* Sci Rep, 2017. **7**(1): p. 995.

37. Nerem, R.S., et al., *Climate-change–driven accelerated sea-level rise detected in the altimeter era.* Proceedings of the national academy of sciences, 2018. **115**(9): p. 2022-2025.

38. Arguez, A., *Indexing, mode definition, and signal extraction in climate research: Analysis and applications involving the MJO, the AO, and ENSO*. 2005, The Florida State University.

39. Cuthbert, M.O., et al., *Observed controls on resilience of groundwater to climate variability in sub-Saharan Africa.* Nature, 2019. **572**(7768): p. 230-234.

40. NASA, *NASA Earth Observatory images by Joshua Stevens, using Landsat data from the U.S. Geological Survey and soil moisture data courtesy of JPL and the SMAP Science Team.* 2018: https://visibleearth.nasa.gov/images/92130/dramatic-flooding-in-eastern-africa/92130f.